

Enhanced Flight Dynamics Models with Aerodynamic Interference for Real-Time Simulation of VTOL Concept Vehicles

Matthew Gladfelter, Chengjian He, and Hossein Saberi
Advanced Rotorcraft Technology, Inc.
Sunnyvale, CA 94085, USA

Carlos Malpica, Wayne Johnson, and Christopher Silva
NASA Ames Research Center
Moffett Field, CA 94035, USA

Abstract

In an effort to establish common models to support the Advanced Air Mobility (AAM) community, NASA has designed a fleet of VTOL configuration reference models. Advanced Rotorcraft Technologies (ART) in cooperation with the NASA Ames Aeromechanics branch has developed FLIGHTLAB simulation models for several of these AAM VTOL concept vehicles. These simulation models are real-time capable while maintaining accurate flight dynamic characteristics with enhanced interference simulation by extracting important modeling parameters from Viscous Vortex Particle Method (VVPM). The focus of this paper is threefold. First, it introduces the simulation models developed and describes their modeling characteristics important to control and flight dynamics simulation. Second, the method for deriving the interference coefficients between model components such as rotors and wings is outlined. Implementation of the method for the lift+cruise and tiltwing models are discussed in detail. Third, the accuracy of the interference enhancement is assessed, with emphasis placed on the impacts to trim and flight dynamic characteristics. The interference enhancement method is further used to evaluate configuration design decisions by quantifying performance aspects of interference. This research effort culminated in simulation models for the AAM VTOL concept vehicles, with proper interference and real-time capability.

Notation

AoA	Angle of attack	N	Number of rotor blades
Azi	Acceleration in inertial z-axis	r	Non-dimensional blade radial position
CSGE	FLIGHTLAB's Control System Graphical Editor	TPP	Rotor tip-path-plane
C_l, C_d, C_m	Lift, drag, and pitch moment coefficients	VVPM	Viscous Vortex Particle Method
C_T	Rotor thrust coefficient	VIO	Uniform inflow velocity
DOF	Degree of freedom	$w(r, \psi, t)$	Rotor inflow over the rotor plane
F_x, F_y, F_z	Force component in x-, y-, z-axis	\vec{w}_{intf}	Rotor induced interference velocity (off-rotor)
H_c	Interference gain matrix for cosine states	x, y, z	Coordinates of flow field point
H_s	Interference gain matrix for sine states	α_1^{0ci}	Uniform induced inflow state of the i th rotor
H_n^m	Radial distribution factor	α_2^{1ci}	Cyclic (cosine) induced inflow state of the i th rotor
IAS	Indicated airspeed	α_2^{1si}	Cyclic (sine) induced inflow state of the i th rotor
m	Harmonic index	$\hat{\alpha}_1^{0ci}$	i th rotor uniform inflow expansion coefficient
n	Radial function index	$\hat{\alpha}_2^{1ci}$	i th rotor cosine inflow expansion coefficient
$(n)!!$	Double factorial of n	$\hat{\alpha}_2^{1si}$	i th rotor sine inflow expansion coefficient
		β	Sideslip angle
		δ_{coll}	Total pilot collective control
		θ_c	Blade collective pitch angle
		θ	Vehicle pitch attitude
		ψ	Rotor azimuth
		$\phi_n^m(r)$	Rotor inflow radial shape function

¹Presented at the Vertical Flight Society's 79th Annual Forum & Technology Display, West Palm Beach, FL, USA, May 16-18, 2023. This is a work of the U.S. Government and is not subject to copyright protection in the U.S.

Introduction

The simulation models discussed are generated from NASA's established fleet of VTOL air vehicle designs for Advanced Air Mobility (AAM) research. These conceptual designs are outlined in Ref. [1] through Ref. [3]. Further discussion of the missions and research focus that these common reference models seek to support can be found in Ref. [4] and [5]. Of the several designs in development, two were selected for this paper. These are the six passenger lift+cruise and tiltwing configurations. Each FLIGHTLAB Ref. [6] simulation model was generated from NDARC Refs. [7] and [8] and OpenVSP Ref. [9] data provided by NASA. The specifications are outlined in Ref. [2] for the lift+cruise vehicle, and Ref. [3] for the tiltwing vehicle. For the lift+cruise configuration, both rotor RPM-controlled and blade pitch collective-controlled variants were constructed and assessed, with results presented in this paper derived from the collective-controlled variant unless otherwise noted.

The FLIGHTLAB simulation models were developed to assess the design viability and evaluate the performance and flight dynamic characteristics, while remaining capable of real-time simulation. To accomplish these goals, a key feature of these simulation models is their use of interference models derived from Viscous Vortex Particle Method (VVPM) simulation data. Previous studies, such as those of Refs. [10] to [12], have shown that VVPM is suitable for advanced multi-rotor inflow and interference simulation, and captures aerodynamic interactions with high accuracy. The computation time, however, makes VVPM unsuitable for real-time applications with current desktop computers. To maintain real-time capability while retaining interference accuracy close to VVPM results, ART developed an approach for enhancing the baseline model interference from the results of VVPM simulation. Similar techniques were implemented Refs. [13] and [14] and shown to be useful for modeling multi-rotor interference. Applicable formulation and experience gained from these studies were adapted and enhanced for the conceptual designs of interest.

To demonstrate the interference calibration method, model development was categorized into baseline, enhanced, and calibrated simulation. The **baseline** model for each configuration was built in FLIGHTLAB for full flight simulation, including rotors, wings (if any), fuselage, aerodynamic surface, landing gear, and

flight controls. The baseline uses Peters-He's finite state wake model, as defined by Ref. [15], to simulate rotor induced inflow dynamics, but does not include rotor-on-rotor interference effects. The **enhanced** models use VVPM instead of dynamic inflow. The enhanced models consist of rotor only models for a cost-effective use of the high fidelity capability of VVPM. The **calibrated** models were obtained from the baseline by integrating the rotor interference data extracted from VVPM simulation. The calibrated models are real-time capable, and may be used for flight dynamic evaluation.

Baseline VTOL Air Vehicle Models

The first task completed was development of baseline simulation models that are capable of real time, but do not include an interference option. The baseline models for the lift+cruise and tiltwing configurations are first described to provide an overview of the configurations and model characteristics, before the interference model enhancement method is explored.

Lift+Cruise

The lift+cruise VTOL configuration consists of a main wing supporting eight lifting rotors, while a pusher propeller located behind the empennage provides forward thrust. The vehicle geometry was verified against NDARC and OpenVSP models, and was derived from the work in Refs. [1] and [2]. Figure 1 shows the simulation model as it has been constructed in FLIGHTLAB, while Fig. 2 outlines the rotor numbering convention. Variants of the baseline vehicle model were developed for torque/RPM-based control and blade collective pitch-based control. These model variants share geometric properties and only differ in control system implementation. The vehicle configurations investigated as part of this study are sized for six passengers including crew. For the analyses presented in this report, the lift+cruise vehicle model is set to a total mass of 5790.5 lbm to be consistent with the NDARC data. Rotors are modeled using blade element formulation and are articulated with stiff flapping dynamics (1.25/rev). At each of 12 aerodynamic segments along rotor blades, airloads are determined as a function of the segment local angle of attack, Mach number, and dynamic pressure. The blade element aerodynamics are modeled with nonlinear and unsteady airloads, and a three state Peters-He dynamic wake model is used for each rotor.

The fuselage models for both lift+cruise and tiltwing

designs use a 6DOF rigid body with aerodynamic forces and moments calculated from table lookup. The fuselage airloads tabulated data of both configurations were the results of CFD runs performed by NASA.

A principal characteristic of the lift+cruise configuration is the ability to transition between a low speed rotor borne control mode and a high speed wing borne control mode. At hover and low airspeed, lift is produced by the eight rotors attached to the main wing by four pylons. For the rotor-borne mode, the RPM-controlled variant is controlled through rotor speed, while the collective-controlled variant is controlled through changing the magnitude of the blade pitch angle of these lifting rotors at set speed. As forward airspeed increases, the main wing will generate lift, unloading the lift rotors. Lifting rotors are stopped when an airspeed threshold is met, putting the vehicle in full wing-borne mode. In this wing-borne state, the main wing produces lift, the pusher propeller produces forward propulsive thrust, and the fixed wing control surfaces of the wing and tail are utilized for flight control. For dynamic evaluation, a simple Stability Augmentation System (SAS) and airspeed hold was added to prevent the model from deviating far from the trim condition. These were included in a simple autopilot model that enables runs that start at hover, go through transition, and reach the cruise mode. Both the SAS and autopilot were modeled in CSGE. The autopilot consists of upper modes for speed hold, altitude hold, and heading hold, as well as the SAS inner loop for stability. The Figure 3 diagram shows the full control system structure with these feedback loops.

The control model in CSGE also includes logic for the transition between modes. This includes rotor stop, which is set to occur when the vehicle reaches 85 knots forward flight speed, and gain scheduling to smooth the control transition across the 85 knot threshold. The control system logic implemented to model rotor stop is illustrated in Figure 4. As the airspeed increases beyond 85 knots, and the main wing with proper pitch angle offloads the rotors, the control system slows down the rotation rate (RPM) of the eight lifting rotors. The control logic then clocks the rotor at zero azimuth along the pylon, completing rotor stop. Finally, the control system brings the blade pitch angle to the minimum drag position.

To improve the airloads for the stopped rotor, the airloads are extracted from tabulated data. They replace the rotor airloads from blade element calculation. The airloads from blade element approach are faded out during the last revolution before rotor stop, and the airloads from tables are faded in. The initial studies were performed with the conservative NDARC stopped

rotor coefficients, while the current implementation uses CFD stopped rotor data generated by ART. The CFD airloads data was generated for a two blade rotor aligned with the boom, with comparable airfoil and twist properties to the lift+cruise lifting rotors. Figure 5 presents the CFD force coefficients for the stopped rotor as functions of angle of attack and sideslip angle, beta, while Figure 6 presents the moments.

To test the transition implementation, the simulation model with autopilot engaged was run starting at hover, flown through transition to a cruise speed of 120 knots, then returned to hover. The model is driven via the autopilot airspeed hold while the altitude hold and SAS loops are engaged. The results from the run are presented in Figure 7. The rotor speed shows that rotor stop is properly engaged at the desired airspeed, and that rotors are restarted successfully. For this transition maneuver, the forces for Rotor 1 are shown in Figure 8 with the x-axis zoomed in on the first transition in which the rotor stops. As the rotor speed reduces to approach rotor stop, the 2/rev oscillations in the forces are apparent. During the final revolution, the rotor model aerodynamic forces are faded out by reducing the effective chord length. Meanwhile the stopped rotor CFD airloads are faded in as hub loads. The total force during rotor stop is thus the aerodynamic forces from the CFD airloads table and the structural loads of the rotor model.

To establish baseline flight characteristics for the simulation, the collective-controlled lift+cruise baseline model was trimmed at 20 knot intervals from hover to 120 knots, with an additional 86 knot condition added to view the trim condition immediately after transition to fixed wing mode. The pilot controls, rotor collective angles, vehicle pitch attitude, and power required as a function of airspeed are shown in Figure 9. Adjustments to the elevator and pusher propeller thrust schedule were made to improve the smoothness of trim characteristics as the vehicle crosses the stopped rotor transition threshold. The vehicle exhibits satisfactory trim characteristics for the respective low speed and high speed modes.

In addition to trim analysis, linear models were generated at various airspeeds. These may be used for design of the control system. Linear models were generated via the perturbation method, in which the partial derivatives of the residuals of generalized equations with respect to states and control inputs are computed. Linear model equations are of the state space form:

$$\{\dot{\mathbf{X}}\} = [\mathbf{F}] * \{\mathbf{X}\} + [\mathbf{G}] * \{\mathbf{U}\} \quad (1)$$

$$\{\mathbf{Y}\} = [\mathbf{H}] * \{\mathbf{X}\} + [\mathbf{D}] * \{\mathbf{U}\} \quad (2)$$

For these equations, $\{X\}$ is the state vector, $\{U\}$ is the control input vector, and $\{Y\}$ is the vector of selected outputs. In the above equations, matrix $[F]$ is the stability or dynamic matrix, $[G]$ is the control matrix, $[H]$ is the output matrix, and $[D]$ is the direct input matrix. For nonlinear systems such as these VTOL configurations, the matrices vary as flight condition changes. As such, both full order and reduced order linear models were generated at several conditions of interest. A 9 state (6 DOF) rigid body linear model was selected as the reduced order model. The linear models were assessed for flight dynamic behavior by comparing responses to their respective nonlinear model counterparts. Responses were generated by applying a doublet input profile to the pilot control of interest and collecting vehicle angular and translational rates over a four second run. The input doublet excitation profile consists of a one second, one percent control stick displacement from trim position for each stage of the doublet. The resulting vehicle responses for the longitudinal stick excitation at hover are presented in Figure 10, and provides an example of evaluation of the time response accuracy in comparison to the nonlinear system response. The vehicle pitch rate, Q , and translational rates are presented for the given control input. The responses of the full order and reduced order linear models are compared to the response of the nonlinear model. The linearized models capture the initial change in pitch rate well, showing that the 9-state reduced order linear model is appropriate for control design. The response check was performed for each control channel and flight condition, and no significant discrepancies between the linear model and nonlinear target were present.

Tiltwing

The tiltwing configuration is an eight rotor vehicle with a main, tilting wing that supports six rotors and a T-tail that supports two rotors. The rotors and hubs attached to the T-tail tilt, but the horizontal tail surface is fixed to the body. As with the other configurations, the vehicle is sized to hold six passengers, including pilots. The total vehicle weight is set to 6715 lbs. Figure 11 shows the tiltwing configuration as constructed in FLIGHTLAB and set to the hover condition where rotors are facing upwards. Figure 12 shows the tiltwing model in the high speed forward flight mode, to illustrate how the wing and rotor components tilt. The NDARC and OpenVSP specifications for the configuration were used to place and size the key components and geometric features. Ideal engine models are used for propulsion.

Each of the eight rotors has five blades and is

modeled using blade element rotor formulation. The rotors are situated to reflect the spacing specified by the OpenVSP model. Rotors are modeled as rigid without flapping dynamics. Given the high blade stiffness, no blade flap or lead-lag DOF was included. The airloads are determined across 16 aerodynamic segments with airfoil properties calculated through table lookup of angle of attack and Mach number. NACA 0012 airfoil data is used for rotor blade airloads. The baseline model utilizes three state Peters-He dynamic wake for induced inflow calculations. Rotor interference effects are not implemented in the baseline model. Rotor blade pitch angles are controlled via a swashplate. The rotors are set to a constant RPM to obtain a tip speed of 550 feet per second for low speed and transition (up to 100 knots), and 300 feet per second for wing borne forward flight. The lifting rotors are attached to the main wing so that rotor loads are transmitted to the fuselage through the wing. Rotor hubs are placed with offset from the wing to account for pylon length. Each pylon's mass is accounted for a point mass located at the pylon center of mass.

The main wing has a tilting mechanism and is the primary lifting surface in forward flight. The wingspan is 43.72 feet with chord and sweep profiles to match NDARC specifications. The wing is modeled with lifting-line and 18 aerodynamic and structural segments. Both the main wing and horizontal tail use the GAW-1 airfoil modified to 18% thickness.

The control system was developed in CSGE with mixing that converts four pilot control (longitudinal, lateral, directional/pedal, and collective) inputs into rotor collective pitch angle and fixed-wing control surface deflections. For the hover and low speed rotor borne mode, the blade collective pitch of all rotors are used to control the aircraft heave motion. Differential collective of the rotors of the main wing and tail are used to control the aircraft pitch. Differential collective of left and right rotors are used to control the roll. Ailerons are used to control the yaw while the wing tilt angle at or close to the 88 degrees hover setting. For the high speed, wing borne mode, traditional fixed-wing control surface deflections are used. In addition to the control mixing, the CSGE control system governs the tiltwing transition logic. The main wing and rear rotor angle are scheduled from airspeed, such that transition reflects characteristics of the NDARC model. The main wing pivots about a point located at 74% chord behind the leading edge of the wing root. The rear rotors tilt about a nacelle joint, with the hub offset updated accordingly. Additionally, the rotor nominal rotation speed and the collective pitch angle bias is scheduled to achieve the desired changes across the transition regime.

$$w_i(r_i, \psi_i, t) = w_{ii}^{self}(r_i, \psi_i, t) + w_{ij}^{intf}(r_i, \psi_i, t) \quad (3)$$

$$w_{ij}^{intf}(r_i, \psi_i, t) = \sum_{m=0}^{\infty} \sum_{n=m+1, m+3, \dots}^{\infty} \phi_n^m(r_i) [\hat{\alpha}_n^{mc}(t) \cos(m\psi_i) + \hat{\alpha}_n^{ms}(t) \sin(m\psi_i)] \quad (4)$$

$$\phi_n^m(r_i) = \sqrt{(2n+1)H_n^m} \sum_{q=m, m+2, \dots}^{n-1} r_i^q \frac{(-1)^{(q-m)/2} (n+q)!!}{(q-m)!!(q+m)!!(n-q-1)!!} \quad (5)$$

Trim characteristics were assessed for the completed baseline tiltwing vehicle. The trim sweep of airspeed is shown in Figure 13 and 14. The elevator, flap, and wing angle schedules originated from NDARC specifications, with adjustments made to avoid large changes in the vehicle pitch attitude during transition. For the elevator specifically, angle is scheduled for rotor borne low airspeeds, and is used as a controlled trim variable at higher speed.

Linear models were generated from the nonlinear baseline tiltwing model at hover and level flight of 150 knots. As with the previous configuration, linear models were generated via the perturbation method. The linear models thus generated are of the matrix form of Equations 1 and 2. Two versions of the linear model were produced and compared. A full linear model includes all states (62 for this configuration), and the reduced order linear model includes only the 9 rigid body states. As with the lift+cruise model, the dynamic responses were checked by comparing a four second, one percent doublet response. An example response for the hover longitudinal channel is shown as Figure 15. For each response tested, the linearized models follow the response of the nonlinear model well, showing that even the reduced order linear models continue to capture the significant state responses for the baseline vehicle.

VVPM Enhancement Methodology

With baseline simulation models established, the next objective was inclusion of the aerodynamic interference in the real-time capable baseline model. The aerodynamic interference model characteristics were obtained from a model with VVPM wake. The approach taken is to first extract important rotor

interference data from the VVPM simulation and then integrate the data into the baseline flight dynamics model. The primary focus of the enhancement methodology is to model rotor interference on other rotors or surfaces. The inflow formulation for a given rotor (with index i) contains the self-induced velocity of the rotor, plus interference contributions from other sources (with rotor or source index j), and is given by Eqn. 3 (Ref. [13]). The interference inflow contribution from another rotor can then be expanded further as Eqn. 4. In this equation, ϕ_n^m is the radial distribution of interference inflow and is expressed as Eqn. 5, where H is expressed as:

$$H_n^m = \frac{(n+m-1)!!(n-m-1)!!}{(n+m)!!(n-m)!!} \quad (6)$$

The inflow radial distribution function (ϕ_n^m) is adopted from the finite state inflow formulation and it is related to Legendre polynomials as derived for proper expansion of rotor induced flow over the rotor plane ([15]). The paired (m n) are the indexes for the interference inflow azimuthal (harmonic) and radial variation, respectively. For example, the first radial distribution associated with the 0th harmonics, $\phi_1^0 = \sqrt{3}$, is simply a uniform variation and the first radial distribution associated with the first harmonics, $\phi_2^1 = \sqrt{7.5} r$, is for a linear variation.

From the formulation of Eqn. 4, the interference velocity associated with j th source can be approximated by selecting appropriate values for the interference expansion coefficients ($\hat{\alpha}_n^{mc}$ and $\hat{\alpha}_n^{ms}$). The primary objective of the VVPM model simulation is to generate interference velocity data from which an appropriate correction can be determined to model the rotor interference. The interference inflow expansion coefficients are extracted from the w_{ij}^{intf} VVPM data and can be related to the thrust of interfering rotor, j , via a variable gain matrix [H], and expressed as Eqn. 7. The gain matrix [H] in Eqn. 7 may be tabulated as a

function of flight condition and is computed from runs of the model with VVPM wake.

$$\hat{\alpha}_n^{mc} = [H_c]C_{Tj} \quad \hat{\alpha}_n^{ms} = [H_s]C_{Tj} \quad (7)$$

The above formulation is applied to each configuration in such a way as to capture the aerodynamic interference. For the lift+cruise model, the interaction of interest is the rotor-on-rotor interference in the rotor-borne mode. More specifically, the interference of forward mounted rotors on rear mounted rotors needs to be computed and included in the baseline model. To do this, two test cases were established to assess the self-induced inflow and rotor-on-rotor interference.

A VVPM isolated lifting rotor model is utilized for improving the accuracy of the self-induced inflow. As shown in Figure 16, only the selected rotor is modeled and run with VVPM. The objective of the investigation is to achieve equivalent rotor power for the same rotor thrust and flight condition between baseline and VVPM models.

Rotor-on-rotor interference is also determined. For the lift+cruise model application, a VVPM tandem rotor model is utilized for this task. As shown in Figure 17, the model with VVPM consists of a forward and rear lifting rotor (rotor 1 and 5, respectively). With this configuration and VVPM, the aerodynamic interference of the forward rotor on rear rotor is computed. The objective is to achieve equivalent interference velocity for rotor 1 on rotor 5 in the baseline model for the same flight condition. The steps used to compare interference velocities between models and set up corrections are as follows:

1. Trim the baseline model to the desired flight condition. For the two rotors of interest, collect the thrust coefficient and induced velocity.
2. Set the isolated multi-rotor model with VVPM to the flight condition of interest (e.g., advance ratio, climb rate, etc.). Run to steady state and collect the rotor thrust and induced velocity.
3. Run the isolated lifting rotor model with VVPM for the prescribed condition of the rotor receiving interference. Determine the self-induced velocity for this rotor.
4. Subtract the self-induced velocity of the isolated single rotor from the induced velocity of the tandem rotor configuration to extract the interference velocity.
5. Using Eqn. 7, extract $\hat{\alpha}_n^{mc}$ and $\hat{\alpha}_n^{ms}$ from the final interference data w.r.t. flight condition.

6. Tabulate H_c and H_s w.r.t. flight conditions.
7. Implement the interference as formulated Eqn. 4 into the baseline model.
8. Verify the implementation by running the calibrated baseline model and comparing to the VVPM simulation.

The tiltwing interference study follows the same approach as established for the lift+cruise rotor-on-rotor interference. For this configuration, the interference to include is that of the wing-mounted rotors on the tail-mounted rotors. Since the aircraft is symmetric about the X-Z plane, only the rotors of one side of this configuration are considered for the enhanced model. The primary difference from the lift+cruise setup is that the VVPM-enhanced tiltwing model consists of four rotors - three wing-mounted rotors and one tail-mounted rotor. This allows for the combined interference of the forward rotors to be captured. Figure 18 shows the schematics of the interaction. Since the VVPM model contains all four rotors for one side, the combined interference velocity is captured, and there is no need to extract the individual interference contributions of each wing-mounted rotor.

The formulation follows Eqn. 3, where $w_{ij}^{intf}(r_i, \psi_i, t)$ will be the combined effect of the three forward rotors. The tables containing the H matrix parameters are set up to model the combined interference effect of the rotors as well. For this configuration, only the uniform interference velocity component is considered.

Lift+Cruise Model Interference Enhancement

The interference calibration method described in the previous section was used to apply VVPM interference characteristics to the baseline lift+cruise model. The isolated lifting rotor model needed for self-induced inflow study is shown in Figure 19 and consists of a single rotor enhanced with VVPM for the purpose of capturing self-induced inflow effects. The isolated rotor model matches the individual lifting rotors of the baseline vehicle model in terms of geometry, blade properties, etc., and is set as counterclockwise to match Rotor 1. For the induced velocity, the VVPM option was selected and a set of interference sample points was created for the comparison of the enhanced model's induced velocity with the baseline results. This set of interference sampling points is provided to

capture induced velocity across the rotor plane from VVPM simulation. The rotor self-induced velocity is then determined, and any difference between the VVPM simulation and baseline model can be removed by introducing the correction factor, kappa, where a kappa value greater than one will reduced the uniform self-induced inflow of the rotor.

The enhanced model with VVPM was run to steady state for conditions of the baseline trim with the same inputs. Figure 20 shows the VVPM wake for the isolated rotor model at the hover flight condition, where velocity was assessed to determine self-induced inflow. The variables of interest for the baseline model with no calibration (kappa = 1.0) and the VVPM rotor model were collected for the hover flight condition and are presented in Table 1. A kappa correction factor of 1.002 was then introduced into the baseline model to improve the uniform velocity, $VI0$, match to VVPM. As shown by the table values, the influence of the kappa correction is very small, and the baseline model self-induced inflow is suitably close to the VVPM values. As such, the self-induced inflow correction was deemed unnecessary, and the research focus was then placed on the rotor-on-rotor interference.

Table 1: Lift+Cruise Self-Induced Inflow

	Baseline, kappa = 1.0	VVPM model	Calibrated, kappa = 1.002
C_T [nd]	0.0175	0.0175	0.0175
$\theta_{c,1}$ [deg]	14.59	14.67	14.59
$VI0$ [ft/sec]	27.22	27.18	27.18

For the inclusion of rotor-on-rotor interference, the tandem rotor configuration was also constructed and tested. This model, as shown in Figure 21, reflects the relative locations of rotors 1 and 5 on the baseline model. Both rotors are coupled with VVPM. The interference sampling point table includes points that span the rotor plane of both rotors, as well as points to investigate interference velocity at the wing and rotor boom.

The models were tested for level flight conditions in 10 knot intervals, up to transition to wing-borne mode, with wake illustrated in Figure 22 for 50 knots. The wake shows that the higher placement of the rear rotor allows it to avoid the primary wake of the forward rotor. Interference data was collected for both the outer and inner rotor spacing, by adjusting the rotor location. Figure 23 describes the difference in spacing. Figure 24 presents the uniform interference velocity for forward rotor on rear rotor as collected from the VVPM tests. For these results, negative values indicate downward interference velocity. The level flight information is displayed as black and blue lines, for outer and inner

rotor pair spacing, respectively. Additional descent cases performed are marked as green points. The level flight velocity information shows the highest interference around 50 knots. The difference in rotor spacing has minimal impact on the interference trend. The descent cases show an increase in interference velocity over their level flight airspeed counterparts. This result is expected given that descending flight moves the front rotor wake closer to the rear rotor plane. Figure 25 shows the VVPM wake for the tandem pair at 50 knots and various descent speeds to illustrate this effect.

The interference velocity information gathered from the VVPM-enhanced model study was used to construct interference tables for $[H]$. These tables follow the methodology of the previous section, with interference correction values dependent on wake skew angle, rate of climb, and sideslip angle to capture the interference dependence on flight condition. For this study, only uniform interference velocity was considered, so Equation 7 simplifies for the uniform inflow expansion coefficient:

$$\hat{\alpha}_1^{0c} = [H]C_{Tj} \quad (8)$$

With the collective-controlled lift+cruise calibrated model constructed, the simulation was run at the flight conditions of the VVPM test matrix to check interference velocities for accuracy. Figure 26 provides a plot of the uniform velocity comparison between models. The calibrated model produces interference velocities that closely match the VVPM targets for both level flight and descent cases.

The next step was to evaluate the accuracy of the interference calibration at flight conditions not directly used for table generation. Both the calibrated model and VVPM-enhanced rotor model were run at 35 and 55 knots level flight, and interference velocities were compared for the influence of Rotor 1 on Rotor 5. Figure 27 presents the data points for the original level flight comparison with the points for 35 and 55 knots added. At these new points, the difference in the interference velocity between the enhanced and calibrated model is slightly higher than directly calibrated points. These differences are small enough to be ignored, and the interference calibration is satisfactory for intermediate airspeeds.

Next, the impact of the rotor-on-rotor interference calibration on vehicle trim was assessed by performing a trim sweep of airspeed. The trim sweep was run for the baseline model with no rotor-on-rotor interference and for the calibrated baseline model. Figure 28 shows the trimmed pilot inputs for level flight across the airspeed envelope, and the resulting vehicle characteristics of rotor collective pitch angle, vehicle

pitch attitude, and power required at trim. These results show that the inclusion of the calibration has a notable impact on the longitudinal trim characteristics prior to transition to the wing-borne mode. The longitudinal stick and collective show up to 10 percent difference in the 30 to 80 knot range to maintain similar vehicle pitch angles, due to the change in rotor effectiveness caused by the interference. There is also a noticeable reduction in performance for this airspeed range, as the power required is higher with interference. Therefore, this study shows the importance of accurate interference modeling on control design and performance.

The impact of the interference calibration was further explored by investigating the frequency domain flight dynamic responses of the models. The vehicle response to pilot control excitations was investigated for baseline and calibrated models at hover and 80 knots. The autopilot loop was used to maintain the flight condition for a 90 second frequency sweep of the pilot input, and the bare airframe response was assessed. No difference in response characteristics was observed at hover, which is expected given the negligible amount of interference. At 80 knots, noticeable difference was observed for the heave response. The response of the vertical acceleration, A_{zi} , to excitation of the collective pilot control is plotted in the frequency domain in Figure 29. The baseline and calibrated models show similar trends in phase and coherence, but the calibrated model has notably smaller magnitude, especially at lower frequencies. This characteristic was attributed to the interference sensitivity to changes in vertical velocity. The collective frequency sweep introduces changes to the amount of interference the rear rotor experiences, which in turn impacts the flight dynamic response for this channel. Sensitivity of heave response to dynamic inflow is noted in other works, such as Ref. [16].

A final investigation performed for the lift+cruise configuration was assessing interference for different tandem rotor configurations. The current configuration has the forward lifting rotors positioned below the wing plane and the rear lifting rotors above. Figure 30 shows the rotor placement from the side view and presents the VVPM wake for the rotor pair at 50 knots level flight. The interference was also determined for a level rotor configuration and a rear rotor low configuration. These options were tested at 50 knots, where the largest magnitude of interference was experienced in the original model. Figure 31 shows the rotor placement and corresponding VVPM wake for the configuration with rotors level (same z-direction location) and positioned above the wing. From the image of the wake, it is observed that the rear lifting rotor is more directly within the wake of

the forward rotor. Figure 32 shows the rotor placement and corresponding VVPM wake for the configuration with forward lifting rotors above the wing plane and rear rotors below. The wake image reveals even more impingement on the rear lifting rotor. The uniform interference velocity on the rear rotor for each configuration was determined from the VVPM data, and is listed in Table 2. The interference data was used to calibrate each configuration, and the resulting impact on the performance of the calibrated model was assessed. As shown in the table, the configuration with the front rotor below and the aft rotor above the wing has the smallest interference velocity and, consequently, the smaller pilot collective and total power required to maintain the trim condition. This finding supports the design decision of the current configuration, from the perspective of rotor-on-rotor interference.

Table 2: Lift+Cruise Rotor Placement Interference Study, 50 knots Level Flight

	Rear Rotor High	Level Rotors	Rear Rotor Low
w_{intf} [ft/s]	13.0	18.9	20.6
δ_{coll} [%]	64.9	69.1	70.3
Power [Hp]	317	332	339

Tiltwing Model Interference Enhancement

The interference enhancement method was also used to calibrate the rotor-on-rotor interference for the tiltwing model. Rotor models with VVPM wake were constructed to analyze the aerodynamic interactions. Due to the vehicle symmetry, four rotors corresponding to one side of the model could be considered. Figure 33 shows an example of the VVPM wake overlaid onto the tiltwing configuration. The rotor model itself is shown in Figure 34. This rotor model shown is set to the hover condition with rotors at 88 degrees wing angle. As with the Lift+Cruise model, level flight and descent cases were chosen to model the interference calibration in terms of variation in wake skew angle and climb rate. For the tiltwing study specifically, the angle of the main wing is an additional critical variable to consider. The change in wing angle both changes the relative spacing of the forward and rear rotors and changes the angle of the wake.

The rotor models with VVPM wake were run for the level flight and descent conditions, and interference

velocity data was collected. The front and side view images of resulting wakes are shown in Figures 35 through 37 for several of the tested conditions. A hover case was run to confirm that negligible interference occurs because of the relatively large separation between the rotors and wakes. The rotors and wakes for this configuration are shown in Figure 35. Figure 36 shows the wake image for the 45 degree wing angle condition. Here, the front rotor wake is nearer to the rear rotor, and a notable amount of interference is experienced. Figure 37 illustrates the wake when the vehicle has fully transitioned to high speed forward level flight.

The uniform interference velocity experienced by the rear rotor is plotted for the conditions tested in Figure 38. Trends for each wing angle position are illustrated by lines of designated color. Descent cases are indicated by diamond points. Similar to the Lift+Cruise model, the maximum interference velocity was experienced during mid-speed transition. These results also show that the combination of the wing angle, airspeed, and flight path angle determines the magnitude of the interference of the front rotors on the tail mounted rotor. Therefore, proper scheduling of wing angle as a function of airspeed and flight path angle is an important variable in the flight management decisions.

The inclusion of the interference similarly accommodates these factors. The data collected from the rotor model with VVPM wake was used to construct the rotor-on-rotor interference calibration tables for $[H]$. The interference correction values are tabulated as a function of wake skew angle, rate of climb, and sideslip angle to capture the interference dependence on flight condition. Additionally, the main wing angle is used as an independent argument for this configuration. Only uniform interference is considered, so the correction follows Eqn. 8.

To check the implementation, the calibrated model was run at the same conditions as the enhanced model, and interference velocities were collected. Figure 39 provides a plot of the uniform interference velocity comparison between calibrated and VVPM models. For these results, negative values indicate downward interference velocity, and the colored lines represent the interference velocity trend for a given model at a given main wing angle. For each flight condition tested, the calibrated model is producing interference velocities that closely match the VVPM targets.

Several descent cases were also included in the calibration table and tested for accuracy. Because the climb rate is included as an independent variable for the calibration table, the interference model accurately reflects the VVPM data for these flight conditions as

well. Figure 40 shows the comparison for the 80 knots descent case alongside the level flight conditions tested at the same wing angle of 30 degrees. The plot shows that the calibrated model matches VVPM results well. Descending flight shows an increase in the interference velocity to the rear rotor. This characteristic is expected given the relative position of wake and the rotors.

Next, additional runs were performed for other flight conditions to further assess the accuracy of the calibration. Both the calibrated model and model with VVPM wake were run at steady level forward flight of 70 knots and 40 degrees wing angle, and 100 knots and 10 degrees wing angle. The comparison of the new data along with the results of the original runs are shown in Figure 41. As seen in the figure, the model with calibrated interference work well for flight conditions in between the points that were used for table generation.

Through further study of low speed flight, it was found that there was no noticeable interference up to 25 knots airspeed with a corresponding wing angle of 68 degrees. This condition was included in the interference table as the threshold of no interference. The VVPM wake image for this flight condition is shown in Figure 42. It can be observed that the wake of the forward rotors is far enough away from the rear rotor to not have any noticeable interference. A second data point for 40 knots level flight airspeed and 60 degrees wing angle was also added to provide additional interference information at low airspeeds and high tilt angles. The VVPM wake is shown in Figure 43. Here, the forward rotor wake begins to influence the rear rotor, and a small amount of interference velocity is observed.

The trim characteristics of the calibrated baseline model were assessed and compared to the baseline model without interference. Figure 44 shows the airspeed sweep of trimmed pilot control positions. The inclusion of the interference calibration adjusted the trimmed longitudinal stick position as much as seven percent in the transition range, and also showed some influence on the collective position. Additional trim results are also shown in this figure, where the interference model shows some influence on the rear rotor collective pitch angle, power required, and pitch attitude of the vehicle. These results show the importance of the inclusion of interference in the flight dynamic model.

Summary and Conclusions

ART in collaboration with NASA has developed and tested simulation models for AAM VTOL concept vehicles. Baseline models, models with Viscous Vortex Particle Method wake, and models with rotor-on-rotor

interference extracted from VVPM for the lift+cruise and tiltwing configurations were constructed and tested. In addition, a methodology was developed to include aerodynamic interactions, while maintaining the ability to run real-time with today's desktop computers. VVPM was run to generate the reference data for the interference enhancements. The overall research accomplishments are summarized as follows:

Baseline blade element models were constructed for the lift+cruise and tiltwing configurations. These models support real-time full flight simulation, and allow for the analysis of flight dynamics, control design, and performance of these VTOL configurations.

Linear models were generated from the nonlinear baseline models for flight conditions of interest. Both full order and reduced order linear models were generated for use in control design refinement. The flight dynamic response of linear models were verified against nonlinear counterparts.

A strategy for enhancing the baseline model via data from VVPM simulation was established and used for each configuration. Models with VVPM were used to generate data for rotor-on-rotor interference. The VVPM interference velocity data was tabulated for use in calibrated models.

The baseline vehicle models were enhanced with the VVPM-derived interference model coefficients. The resulting enhanced/calibrated models were checked to ensure that the interference velocities are consistent with the results from VVPM. Finally, the models with calibrated interference were analyzed to reveal impacts on trim and performance.

Acknowledgment

This research was sponsored by the NASA SBIR program under contract 80NSSC21C0610. Carlos Malpica (Aeromechanics Office, NASA Ames) was the technical monitor.

References

- [1] Wayne Johnson, Christopher Silva, and Eduardo Solis. "Concept Vehicles for VTOL Air Taxi Operations," *AHS Technical Conference on Aeromechanics Design for Transformative Vertical Flight*, San Francisco, CA, January 2018.
- [2] Christopher Silva, Wayne Johnson, Kevin Antcliff, and Michael Patterson. "VTOL Urban Air Mobility Concept Vehicles for Technology Development," *2018 Aviation Technology, Integration, and Operations Conference*, Atlanta, GA, June 2018.

- [3] S. Whiteside, B. Pollard, K. Antcliff, N. Zawodny, X. Fei, C. Silva, and G. Medina. "Design of a Tiltwing Concept Vehicle for Urban Air Mobility," NASA STI Program Report Series, NASA/TM-20210017971, June 2021.
- [4] M.D. Patterson, K.R. Antcliff, and L.W. Kohlman. "A Proposed Approach to Studying Urban Air Mobility Missions Including an Initial Exploration of Mission Requirements," *AHS International 74th Annual Forum and Technology Display*, Phoenix, AZ, 2018.
- [5] K.R. Antcliff, S. Whiteside, L.W. Kohlman, and C. Silva. "Baseline Assumptions and Future Research Areas for Urban Air Mobility Vehicles," *AIAA SciTech Forum and Exposition*, Dallas, TX, 2019.
- [6] Du Val, R. and He, Chengjian, "FLIGHTLAB Modeling for Real-Time Simulation Applications," *International Journal of Modeling, Simulation, and Scientific Computing*, Vol. 8, No. 4, 2017.
- [7] Wayne Johnson. "NDARC NASA Design and Analysis of Rotorcraft," *NASA/TP-2015-218751*, NASA, Moffett Field, CA, 2015.
- [8] Wayne Johnson. "NDARC NASA Design and Analysis of Rotorcraft - Theory," NASA, Moffett Field, CA, April 2019.
- [9] Robert A. McDonald and James R. Gloude-mans. "Open Vehicle Sketch Pad: An Open Source Parametric Geometry and Analysis jTool for Conceptual Aircraft Design," *AIAA 2022-0004, AIAA SciTech 2022 Forum*, January 2022.
- [10] Chengjian He and J. Zhao. "Modeling Rotor Wake Dynamics with Viscous Vortex Particle Method," *AIAA Journal*, 47(4), April 2009.
- [11] Chengjian He and N. Rajmohan. "Modeling the Aerodynamic Interaction of Multiple Rotor Vehicles and Compound Rotorcraft with Viscous Vortex Particle Method," *American Helicopter Society 72nd Annual Forum*, West Palm Beach, FL, May 2016.
- [12] J. Kim, Chengjian He and Jan Goericke, "Modeling and Analysis of eVTOL Air Vehicle Interactional Aerodynamics and Mission Performance," VFS Aeromechanics for Advanced Vertical Flight Technical Meeting, San Jose, CA, January 21-23, 2020.
- [13] Chengjian He, Matt Gladfelder, Chongseok Chang, Mark Tishler, and Ondrej Juhasz. "VPM-Derived State Space Inflow Model for Multi-Rotor Air Vehicle Modeling and Simulation," *Vertical Flight Society 75th Annual Forum*, Philadelphia, PA, May 2019.

- [14] Matt Gladfelter, Chengjian He, Chongseok Chang, Mark Tishler, Mark Lopez, and Ondrej Juhasz. "Enhancement and Validation of VPM-Derived State-Space Inflow Models for Multi-Rotor Simulation," *Vertical Flight Society 76th Annual Forum*, Virtual, Oct 2020.
- [15] Peters, D. A. and He, Chengjian, "Finite State Induced Flow Models Part II: Three Dimensional Rotor Disk," *Journal of Aircraft*, Vol. 32, No. 2, March-April, 1995, pp. 323-333.
- [16] Chen, Robert T.N. and Hindson, William S., "Influence of Dynamic Inflow on the Helicopter Vertical Response," NASA/TM-88327, June, 1986.

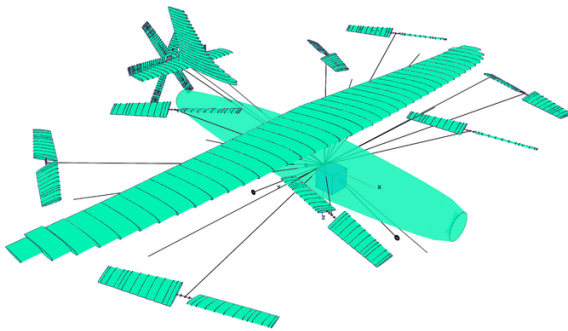


Figure 1: Lift+Cruise FLIGHTLAB Vehicle Model

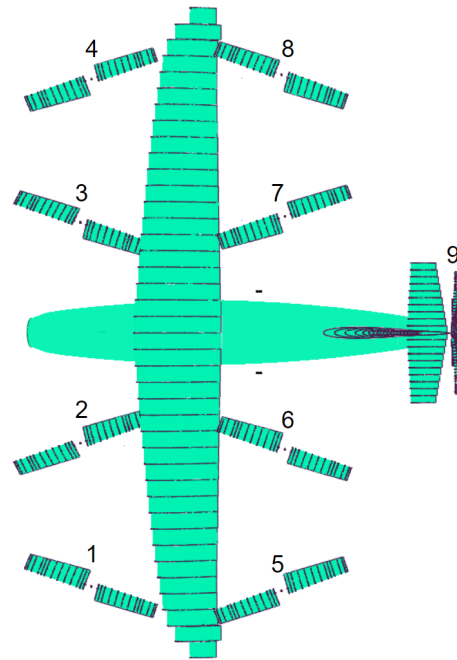


Figure 2: Lift+Cruise Rotor Numbering Convention

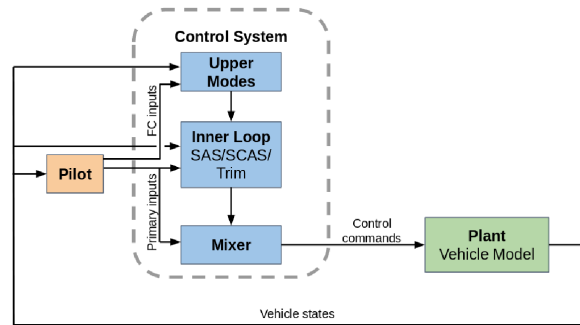


Figure 3: Control System Full Structure

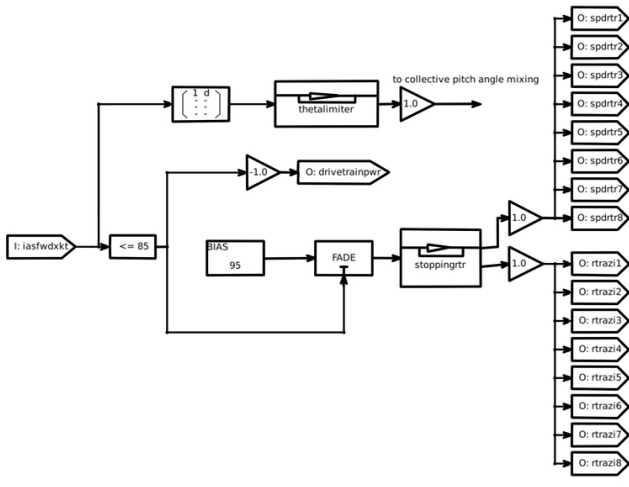


Figure 4: Stopped Rotor CSGE Logic

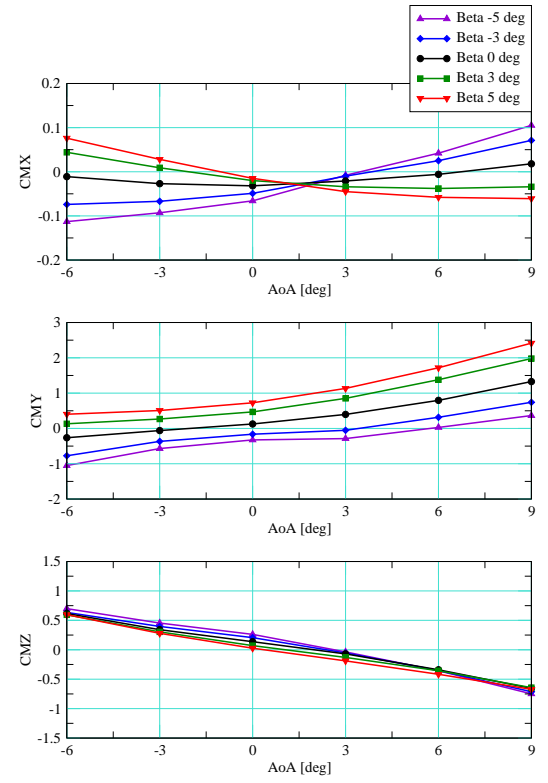


Figure 6: Stopped Rotor Moment Coefficients from CFD

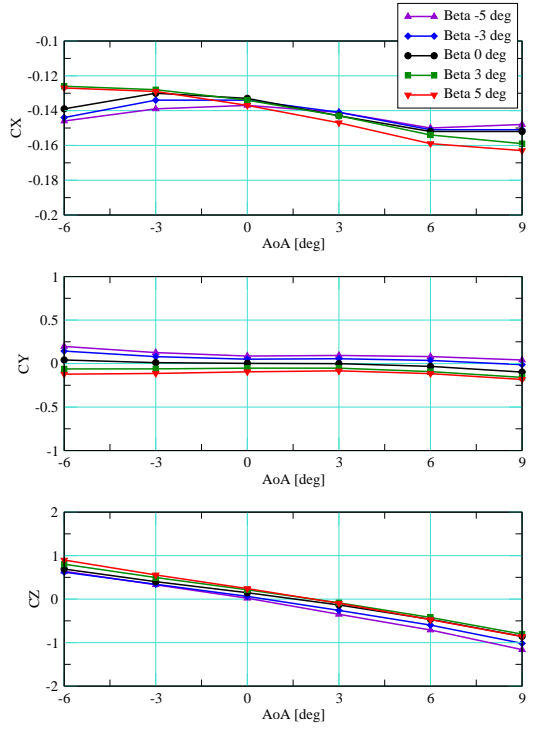


Figure 5: Stopped Rotor Force Coefficients from CFD

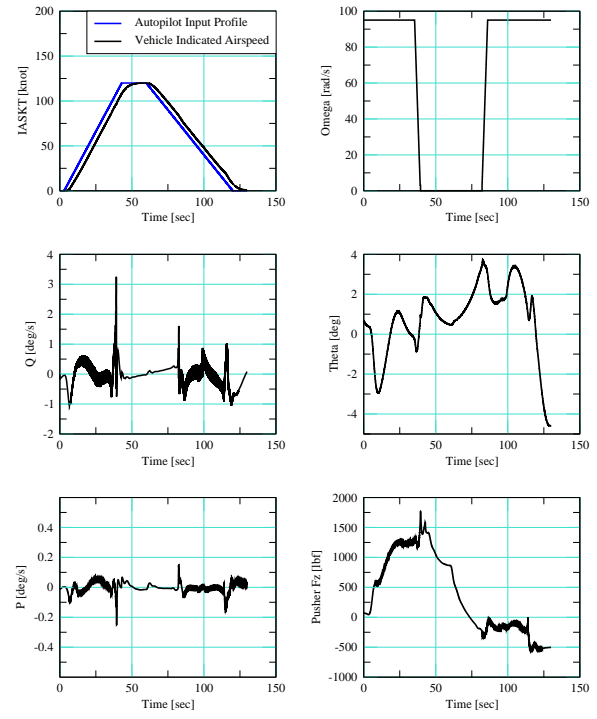


Figure 7: Results from Flight through Transition

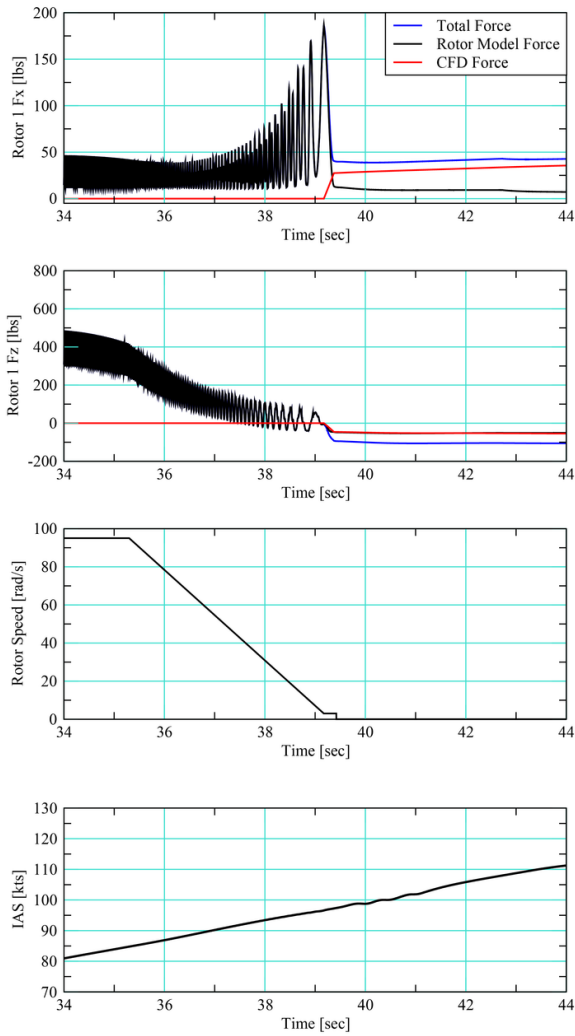


Figure 8: Rotor Forces during Transition to Stopped Rotor

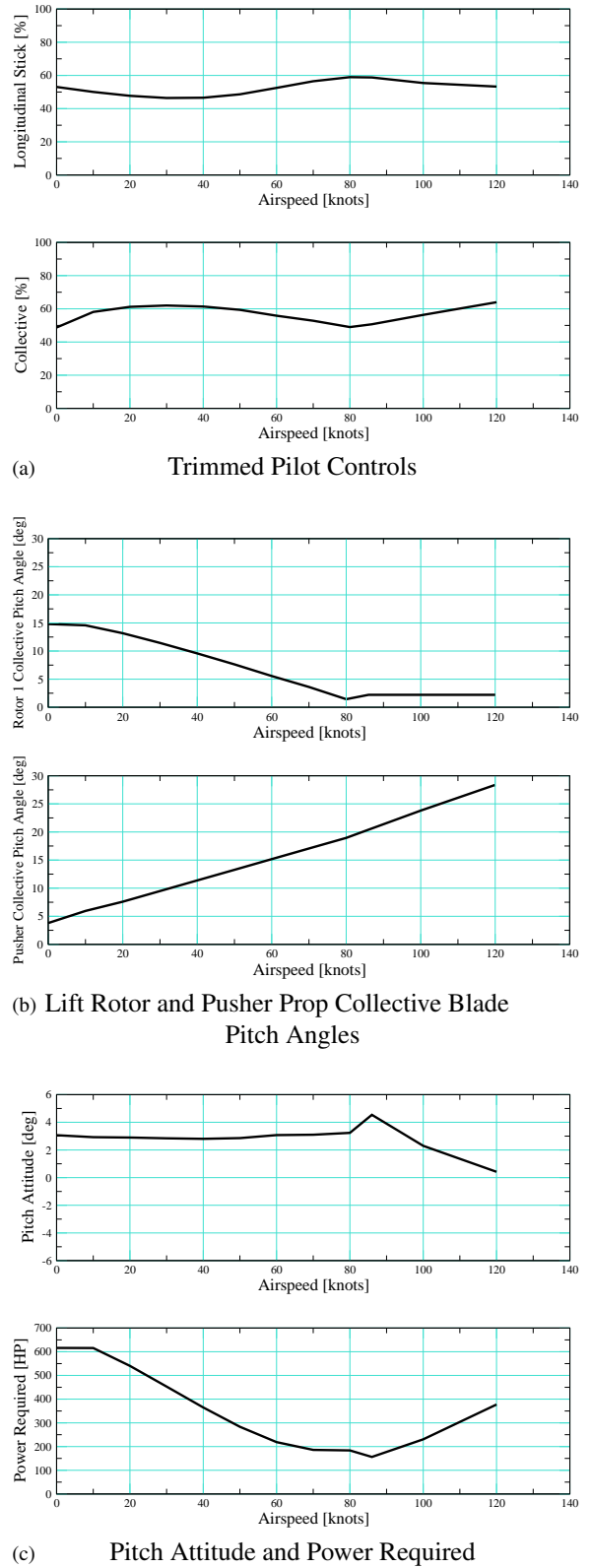


Figure 9: Lift+Cruise Trim Results for Baseline Model

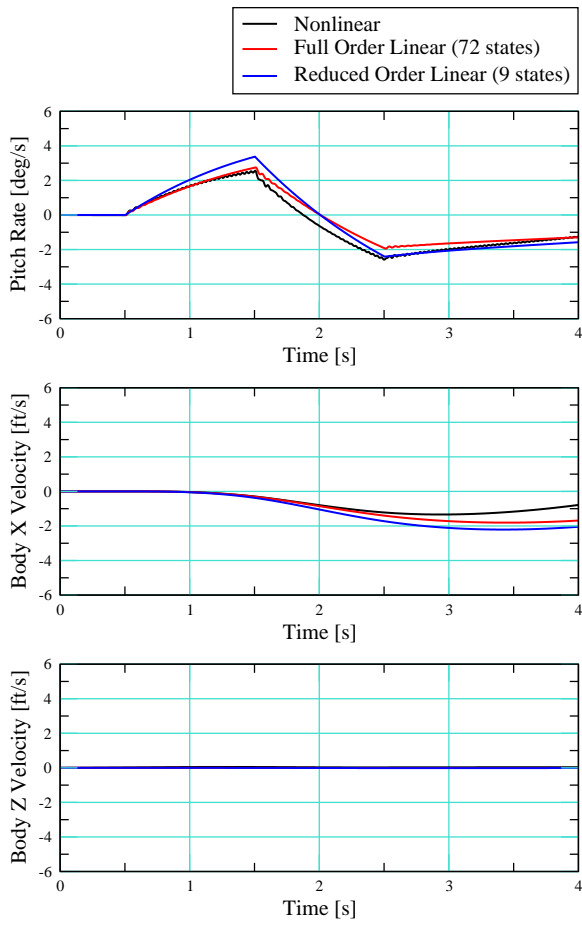


Figure 10: Lift+Cruise Baseline Dynamic Response to Longitudinal Input at Hover

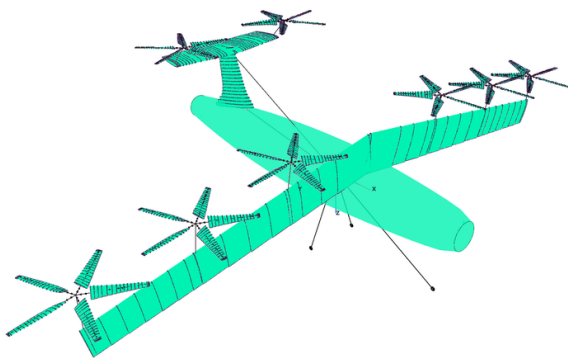


Figure 11: Tiltwing FLIGHTLAB Model in Hover

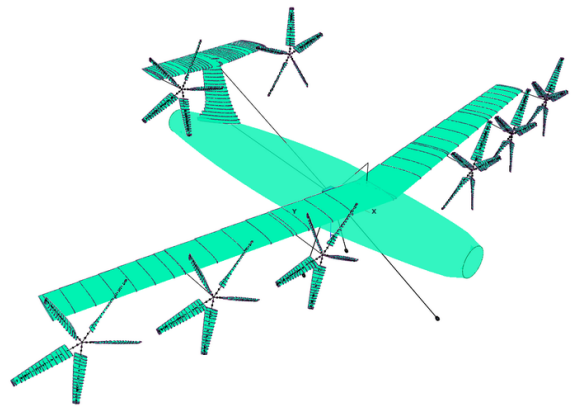


Figure 12: Tiltwing FLIGHTLAB Model in Forward Flight

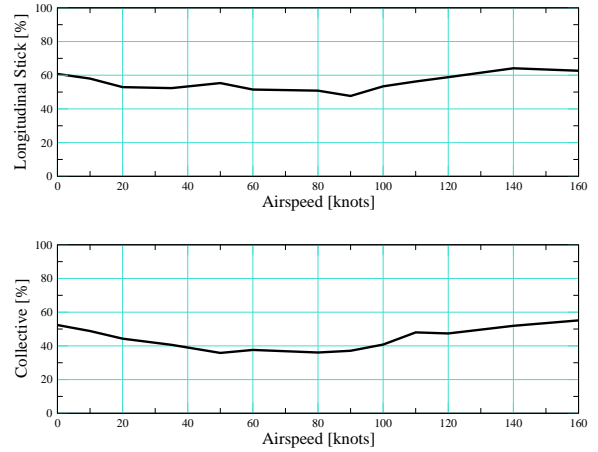


Figure 13: Tiltwing Baseline Model Trimmed Pilot Controls

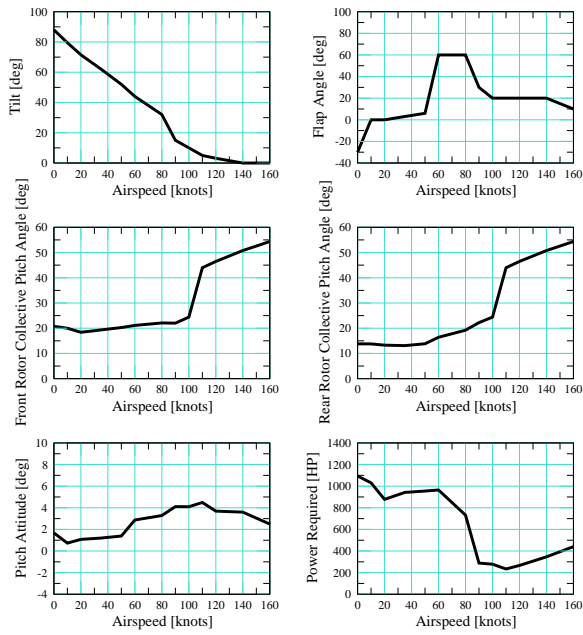


Figure 14: Tiltwing Trim Results for Baseline Model

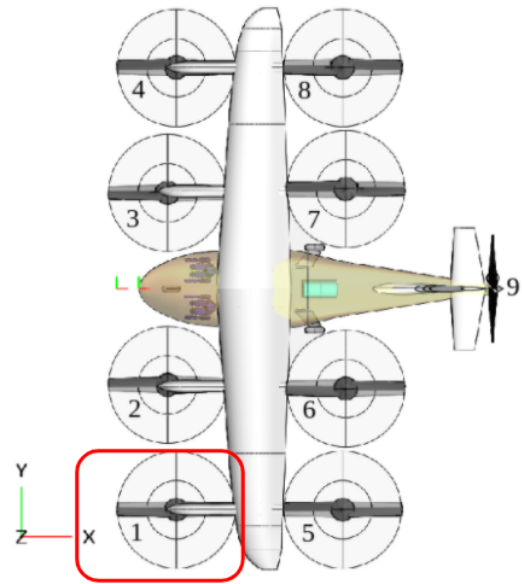


Figure 16: Lift+Cruise Enhancement from VVPM Case 1: Self-Induced Inflow

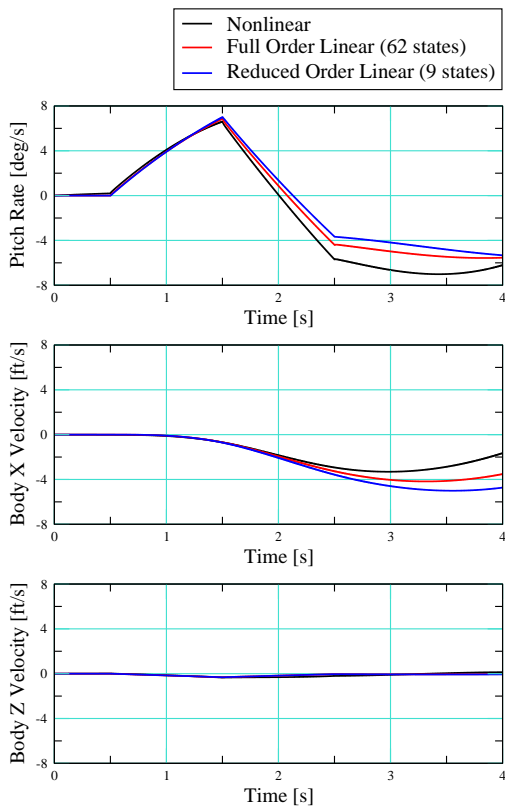


Figure 15: Tiltwing Baseline Model Dynamic Response to Longitudinal Input at Hover

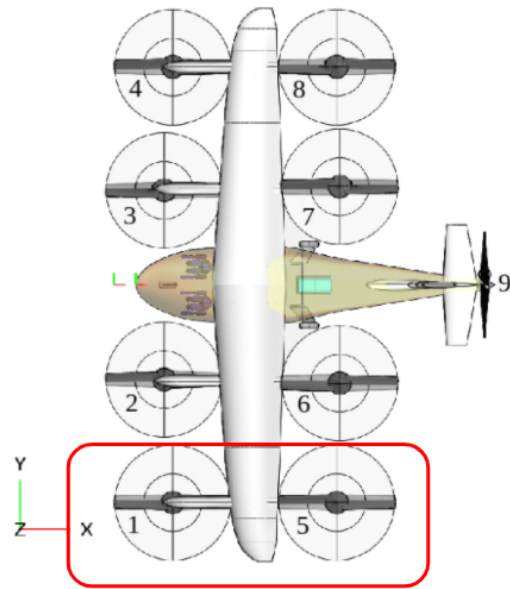


Figure 17: Lift+Cruise Enhancement from VVPM Case 2: Rotor-on-Rotor Interference of Tandem Rotors

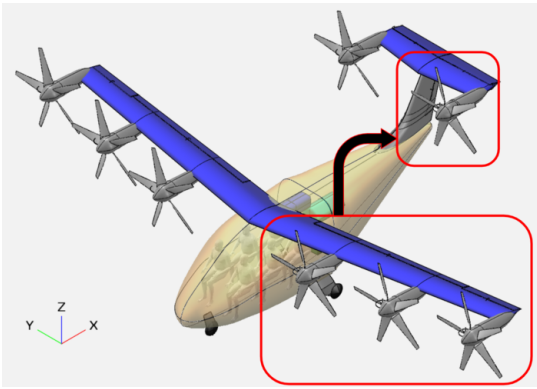


Figure 18: Tiltwing Enhancement from VVPM: Forward Rotor Interference on Rear

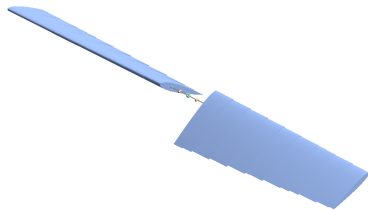


Figure 19: Lift+Cruise Isolated Lifting Rotor Model

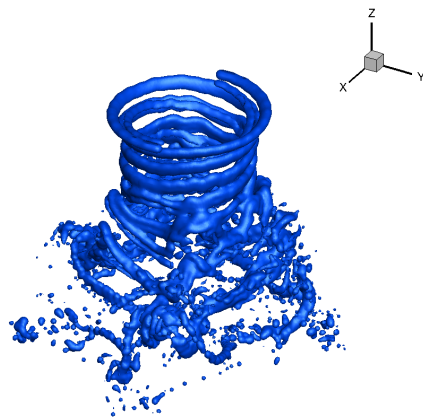


Figure 20: VVPM Wake for Isolated Lifting Rotor at Hover

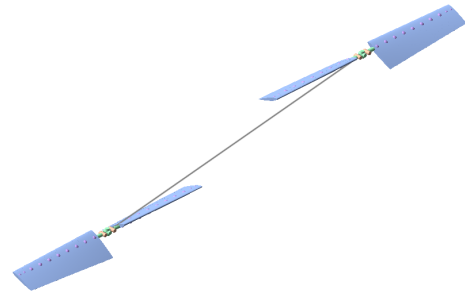


Figure 21: Lift+Cruise Tandem Lifting Rotors Model

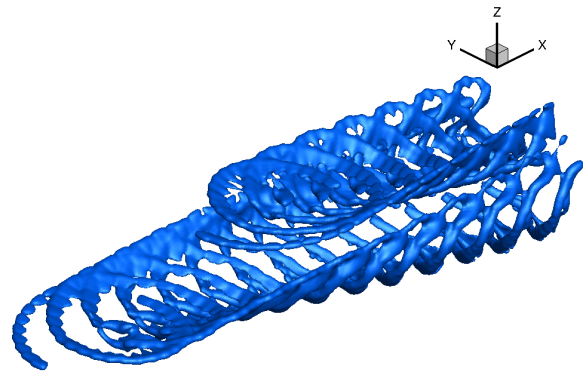


Figure 22: VVPM Wake of Lift+Cruise for a Tandem Lifting Rotor Pair at 50 knots

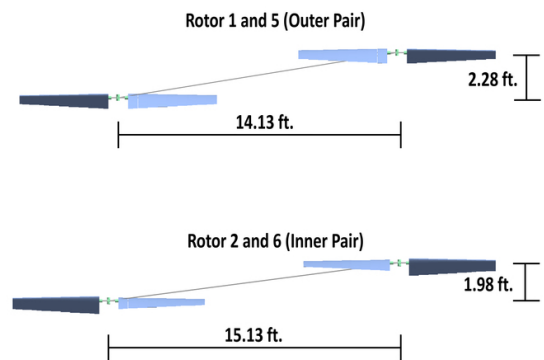


Figure 23: Rotor Spacing for Inner and Outer Tandem Pairs

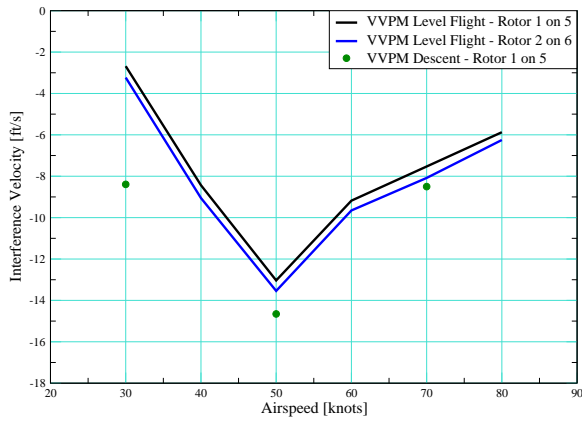


Figure 24: Lift+Cruise VVPM Model Rotor-on-Rotor Interference Velocity

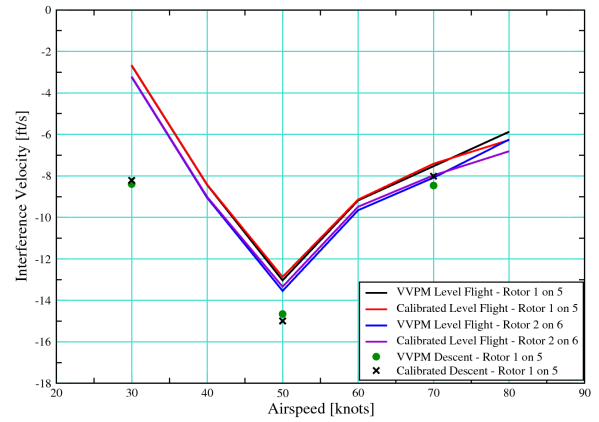


Figure 26: Lift+Cruise Rotor-on-Rotor Interference Velocity Comparison

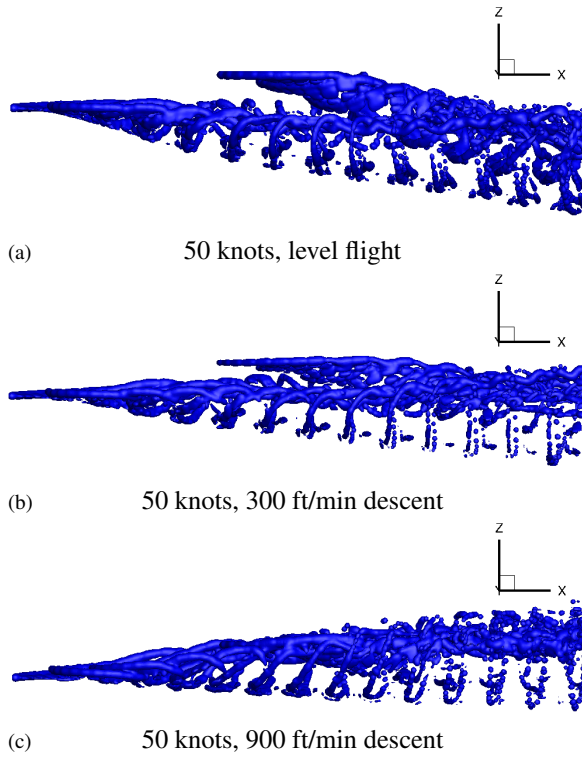


Figure 25: VVPM Wake for Tandem Rotors at Various Descent Rates

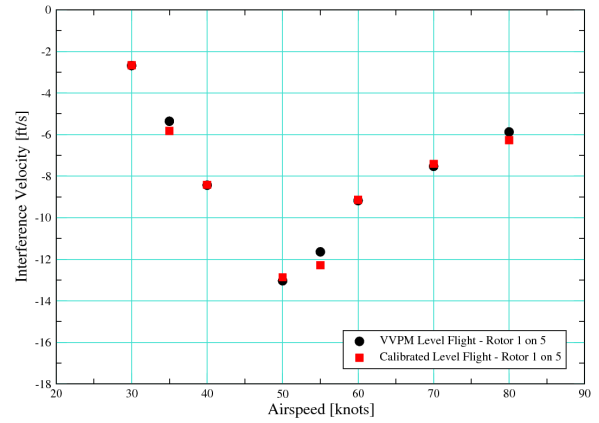
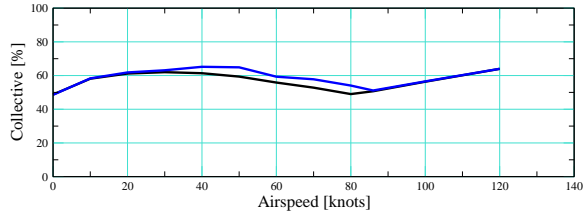
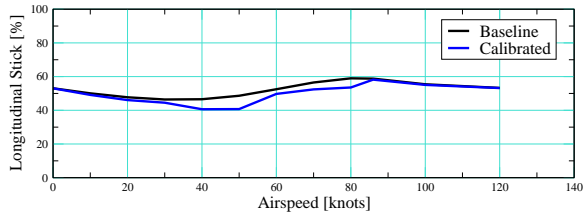
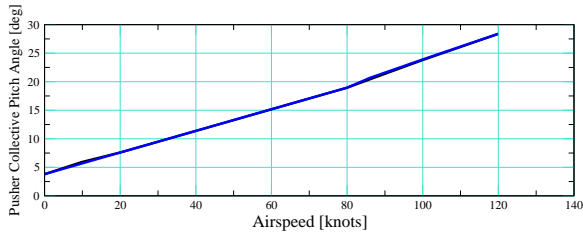
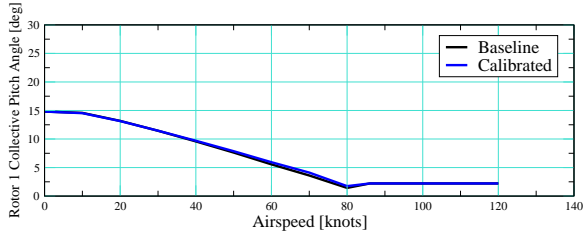


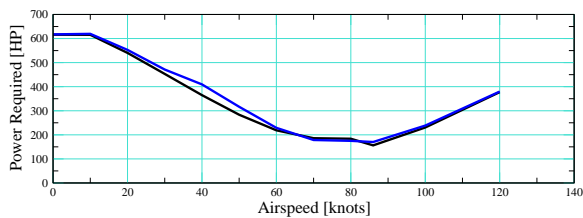
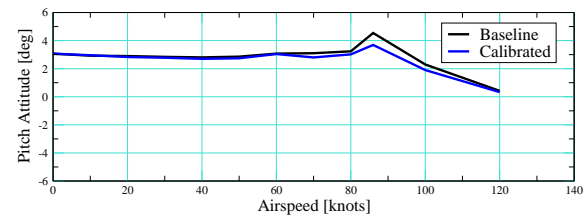
Figure 27: Lift+Cruise Rotor-on-Rotor Interference Velocity Comparison with Additional Flight Conditions



(a) Trimmed Pilot Controls



(b) Rotor Collective Pitch Angles



(c) Pitch Attitude and Power Required

Figure 28: Lift+Cruise Trim Results for Baseline (no-interference) and Calibrated Models

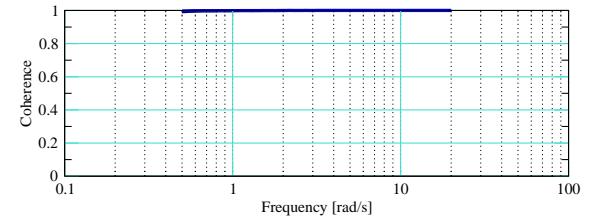
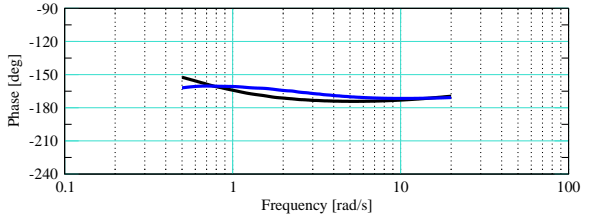
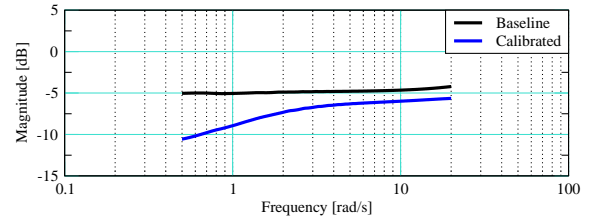
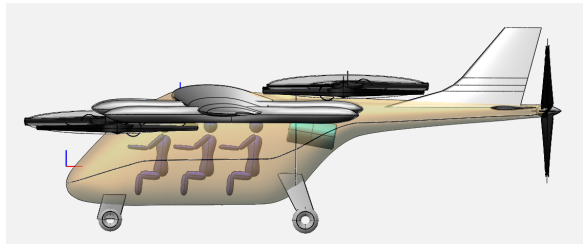
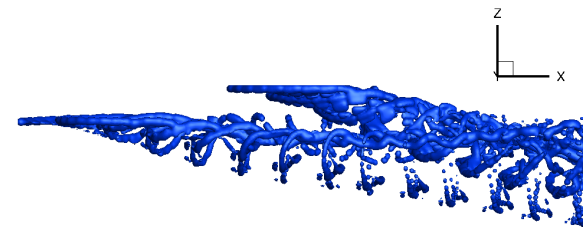


Figure 29: Lift+Cruise Heave Response to Collective Frequency Sweep, Azi/δ_{coll} , 80 knots

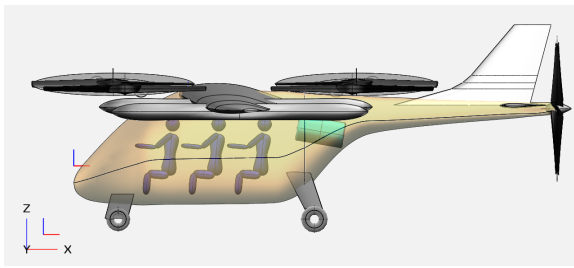


(a) Rotor Configuration

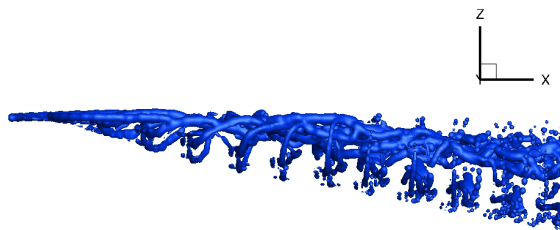


(b) VVPM Wake

Figure 30: VVPM Wake for Rear Rotor High Configuration at 50 knots



(a) Rotor Configuration



(b) VVPM Wake

Figure 31: VVPM Wake for Rear Rotor Level Configuration at 50 knots

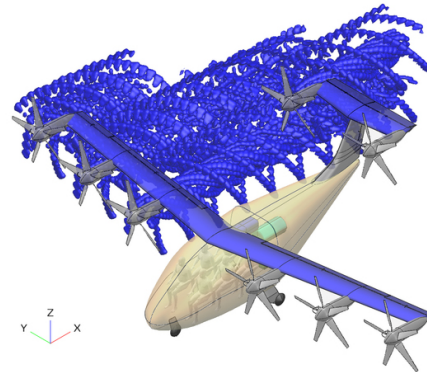
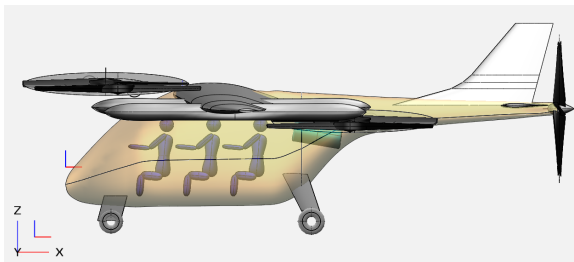
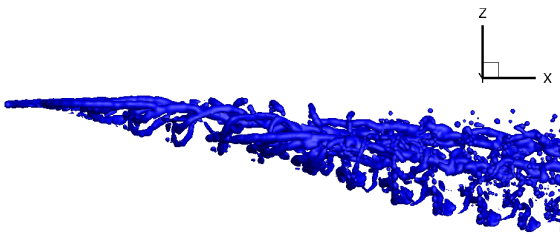


Figure 33: Tiltwing Configuration with VVPM Wake Overlay



(a) Rotor Configuration



(b) VVPM Wake

Figure 32: VVPM Wake for Rear Rotor Low Configuration at 50 knots

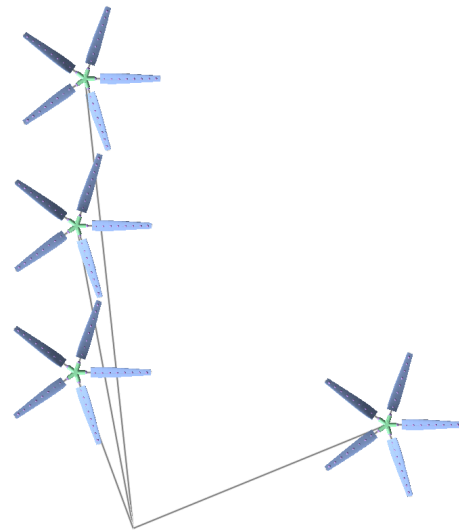


Figure 34: Top view of VVPM Tiltwing Rotor Model set to Hover Flight Condition

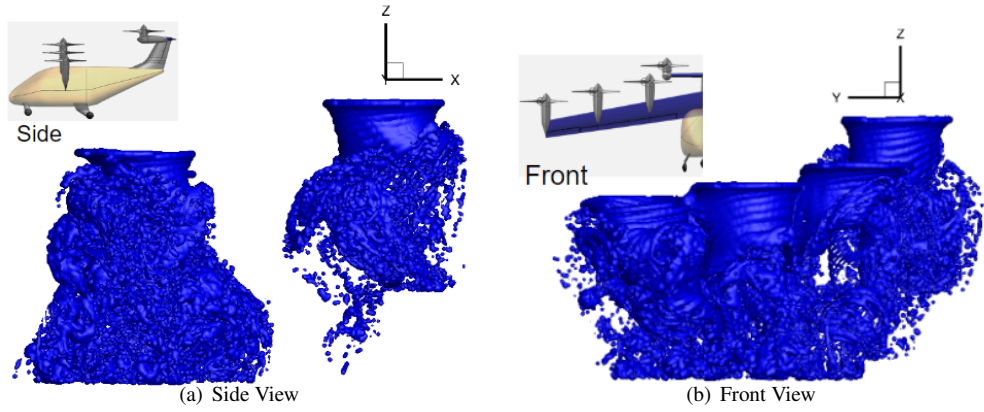


Figure 35: Tiltwing VVPM Wake at Hover, 90 deg Wing Angle

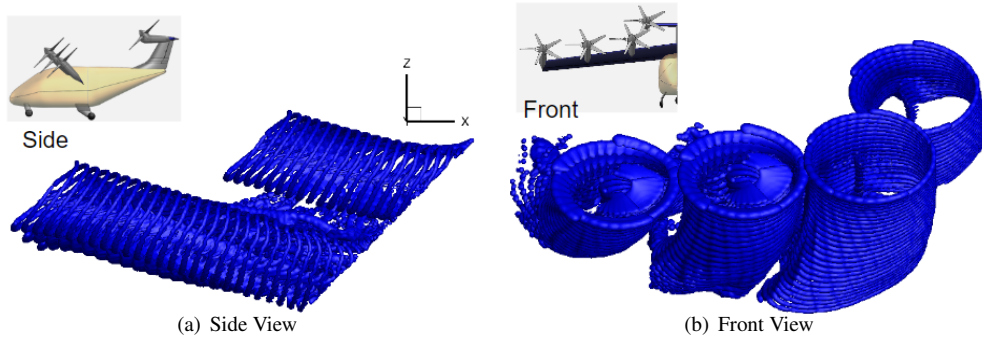


Figure 36: Tiltwing VVPM Wake at 50 knots, 45 deg Wing Angle

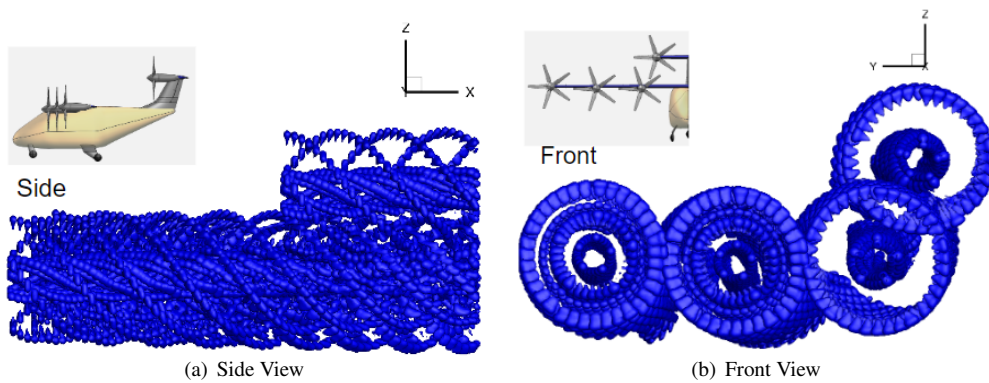


Figure 37: Tiltwing VVPM Wake at 120 knots, 0 deg Wing Angle

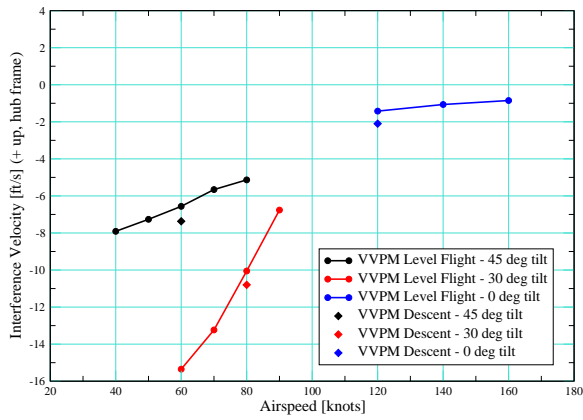


Figure 38: Tiltwing Model with VVPM Wake Rotor-on-Rotor Interference Velocity on Rear Rotor

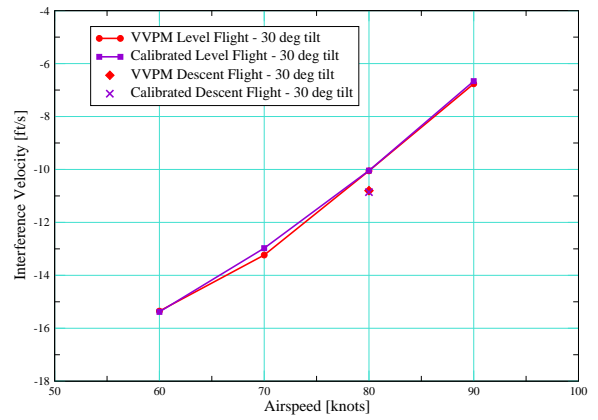


Figure 40: Tiltwing Rotor-on-Rotor Interference Velocity Including Descent

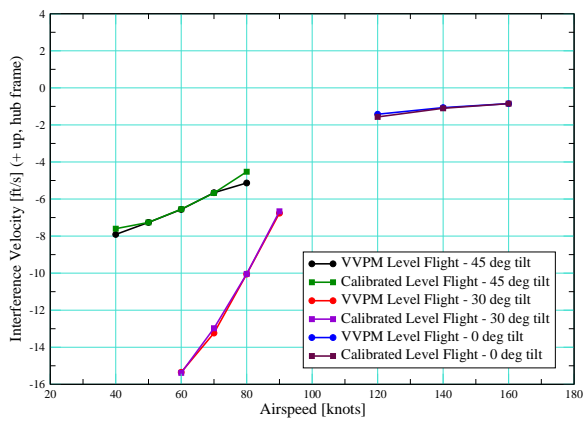


Figure 39: Tiltwing Rotor-on-Rotor Interference Velocity Comparison

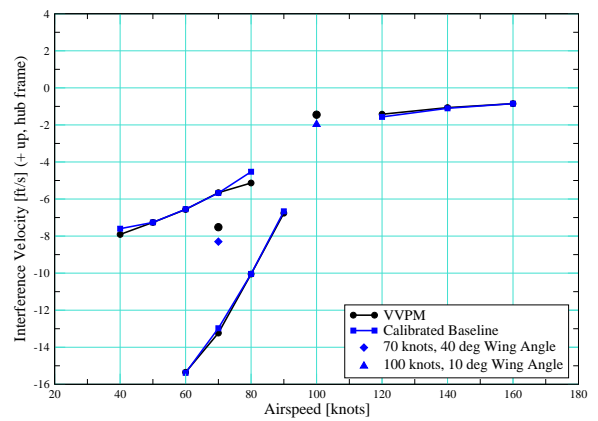
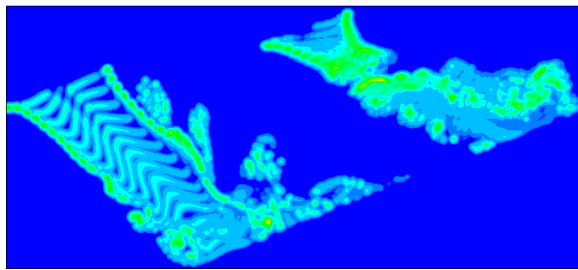
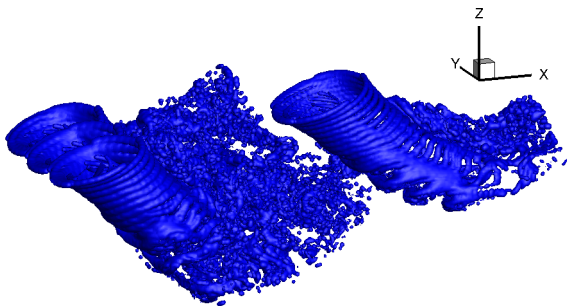


Figure 41: Tiltwing Rotor-on-Rotor Interference Velocity Comparison with Additional Flight Conditions

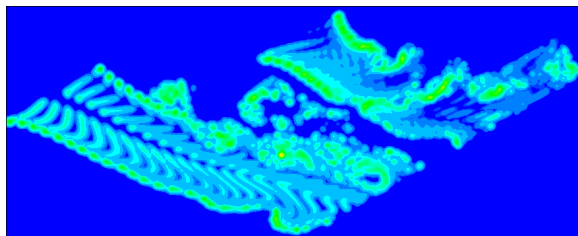


(a) VVPM Slice

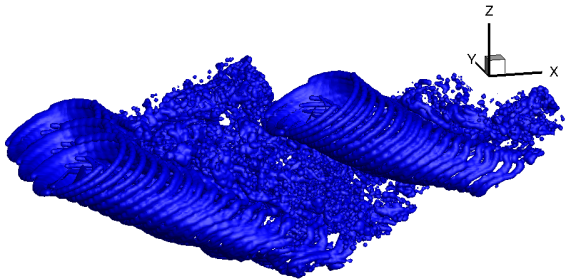


(b) VVPM Wake

Figure 42: Tiltwing VVPM Wake at 25 knots, 68 deg Wing Angle

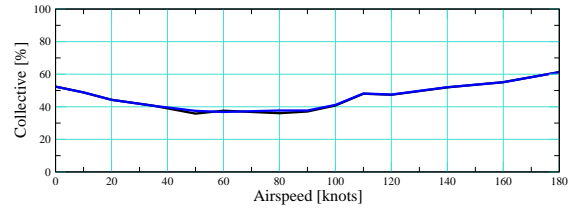
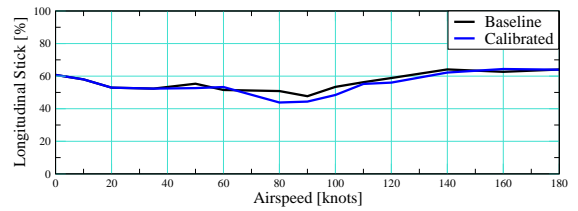


(a) VVPM Slice

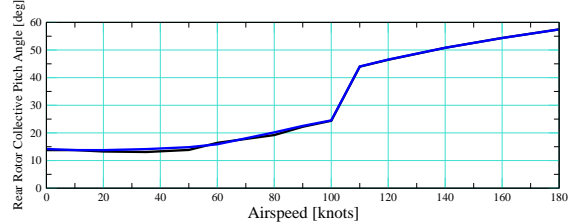
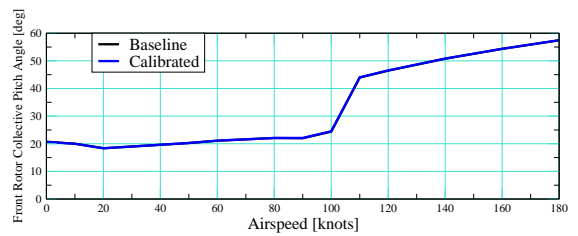


(b) VVPM Wake

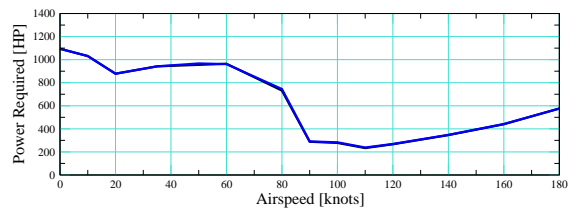
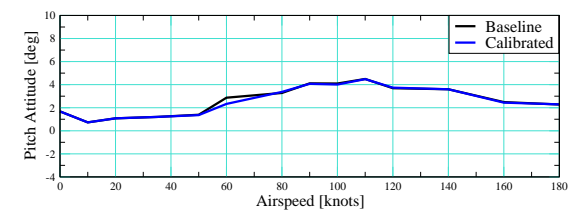
Figure 43: Tiltwing VVPM Wake at 40 knots, 60 deg Wing Angle



(a) Trimmed Pilot Controls



(b) Rotor Collective Pitch Angles



(c) Pitch Attitude and Power Required

Figure 44: Tiltwing Trim Results for Baseline (no-interference) and Calibrated Models